

## Sensitivity of simulated Arctic sea ice to realistic ice thickness distributions and snow parameterizations

K. Castro-Morales,<sup>1</sup> F. Kauker,<sup>1</sup> M. Losch,<sup>1</sup> S. Hendricks,<sup>1</sup> K. Riemann-Campe,<sup>1</sup> and R. Gerdes<sup>1</sup>

Received 7 August 2013; revised 21 November 2013; accepted 21 December 2013.

[1] Sea ice and snow on sea ice to a large extent determine the surface heat budget in the Arctic Ocean. In spite of the advances in modeling sea-ice thermodynamics, a good number of models still rely on simple parameterizations of the thermodynamics of ice and snow. Based on simulations with an Arctic sea-ice model coupled to an ocean general circulation model, we analyzed the impact of changing two sea-ice parameterizations: (1) the prescribed ice thickness distribution (ITD) for surface heat budget calculations, and (2) the description of the snow layer. For the former, we prescribed a realistic ITD derived from airborne electromagnetic induction sounding measurements. For the latter, two different types of parameterizations were tested: (1) snow thickness independent of the sea-ice thickness below, and (2) a distribution proportional to the prescribed ITD. Our results show that changing the ITD from seven uniform categories to fifteen nonuniform categories derived from field measurements, and distributing the snow layer according to the ITD, leads to an increase in average Arctic-wide ice thickness by 0.56 m and an increase by 1 m in the Canadian Arctic Archipelago and Canadian Basin. This increase is found to be a direct consequence of 524 km<sup>3</sup> extra thermodynamic growth during the months of ice formation (January, February, and March). Our results emphasize that these parameterizations are a key factor in sea-ice modeling to improve the representation of the sea-ice energy balance.

**Citation:** Castro-Morales, K., F. Kauker, M. Losch, S. Hendricks, K. Riemann-Campe, and R. Gerdes (2014), Sensitivity of simulated Arctic sea ice to realistic ice thickness distributions and snow parameterizations, *J. Geophys. Res.*, 119, doi:10.1002/2013JC009342.

### 1. Introduction

[2] Sea ice is a complex system that forms the interface between the atmosphere and the ocean: it insulates the ocean against heat transfer to and from the atmosphere, and contributes to the ice-albedo feedback mechanism. Because of these effects, the rapid decrease of Arctic summer sea-ice extent and thickness in recent years [Serreze *et al.*, 2003, 2007b; Stroeve *et al.*, 2008, 2011; Winton, 2011] contributes to the polar amplification of global climate change [Serreze *et al.*, 2009]. Representing these changes accurately in numerical models is still a challenge.

[3] Nowadays, most sea-ice model codes resolve both dynamic (movement and deformation of the ice) and thermodynamic (transfer of heat or radiation) processes. Sea-ice momentum equations with specific rheologies [Kreyscher *et al.*, 2000] are solved for drift velocities that are used to advect the ice and snow variables. Thermodynamic processes are used to determine ice growth and decay due to melting and freezing. Many simple sea-ice

models, such as our model, resolve only two thickness categories: open water (thin ice and open water) and sea ice [Hibler, 1979]. Ice thermodynamics, however, depend strongly on ice and snow thicknesses. These quantities can vary considerably on scales smaller than the model's grid cell size. In order to parameterize these subgrid-scale variations, the mean sea-ice thickness ( $h_i$ ) is often replaced by an ice thickness distribution (ITD). The ITD is represented as a probability density function  $g(h)$  [Thorndike *et al.*, 1975].

[4] In practice, this distribution function is discretized. Some sea-ice models, such as the one used here, work with the assumption that the distribution is fixed in time. Often, this distribution is flat, that is, it uses the same probability for all thickness categories [Hibler, 1984] (see gray bars in Figures 1a and 1b).

[5] It has been shown that the distribution of ice thicknesses over an ice covered area is nonuniform with one to sometimes three modes [Eicken and Lange, 1989; Lange and Eicken, 1991; Wadhams, 1981]. Thickness distributions also vary with regions and seasons. Bimodal distributions are found in dynamic regions such as Fram Strait, and broad modes in regions such as north of Greenland where new ice or open water are rare throughout the year [Haas *et al.*, 2010]. These observations and the sensitivity of the ocean heat loss through a given ice thickness, suggest that a dynamic nonhomogeneous and multicategory ice thickness distribution is required to describe sea ice in numerical models.

<sup>1</sup>Alfred Wegener Institute, Helmholtz Centre for Polar and Marine Research, Bremerhaven, Germany.

Corresponding author: K. Castro-Morales, Alfred Wegener Institute, Helmholtz Centre for Polar and Marine Research, Bremerhaven 27570, Germany. (karel.castro-morales@awi.de)

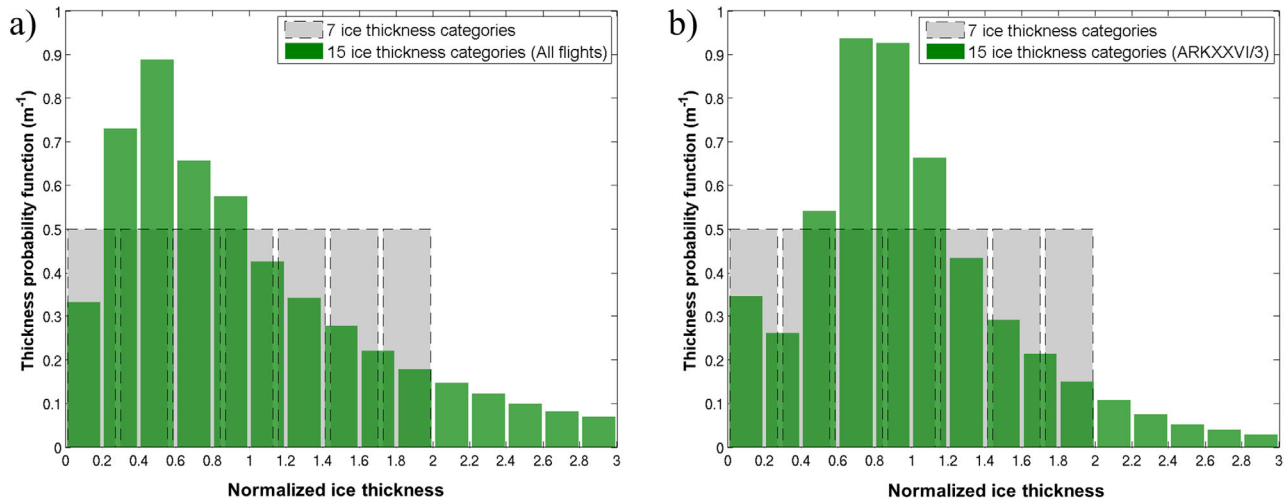


**Figure 1.** The ice thickness distributions based on airborne EM-bird measurements: (a) from a compilation of 19 campaigns (112 flights) and (b) from one field campaign (ARKXXVI/3). The canonical seven categories uniformly distributed are shown in gray. All ITDs are scaled to give a mean thickness of 1 m.

[6] Since both thermodynamic and dynamic processes depend on ice thickness, it is important to have a representation of thickness variations below the grid scale in a sea-ice model [Hunke *et al.*, 2010]. Consequently, more sophisticated models now evolve the ITD over time and space and redistribute ice between categories according to redistribution functions. More recent “dynamic” ITD models, e.g., CICE (Los Alamos Sea-Ice Model, sea-ice component of the Community Earth System Model, CESM) [Hunke and Bitz, 2009], TED (Thickness and Enthalpy Distribution) [Zhang and Rothrock, 2001], and LIM3 (Louvain-la-Neuve) [Vancoppenolle *et al.*, 2009], carry a time varying thickness distribution with an ice concentration for each ice category within a grid cell and hence, increase the thermodynamic resolution [Hunke *et al.*, 2010].

[7] Although dynamic ITD models appear more physical, they still require assumptions about the redistribution between ice categories and there are hardly enough observational data available to constrain the details of the redistribution between the ice categories. This and the additional computational cost incurred by advecting many ice thicknesses and concentrations, may be the reason why there are still a number of sea-ice models, including the ice components of some of the CMIP5 models used for the IPCC assessment report, that rely on fixed ITDs following Hibler [1984].

[8] The heat transfer through ice (i.e., the conductive heat flux,  $F_c$ ) critically depends on its thickness, so that the form of the prescribed ITD in the models determines to a large extent the overall heat flux. The description of the thin ice categories is particularly important since the heat fluxes are the largest through these categories. Here we aim to improve the description of the static ITD at low additional computational cost by deriving it from field measurements of ice thickness retrieved from airborne electromagnetic induction sounding measurements (EM-bird) [Haas *et al.*, 2010]. The new static ITD contains more ice categories (15) than in the canonical configuration and follow a nonuniform distribution that resolves thin ice more accurately (Figure 1).

[9] The snow cover on top of the ice is as important as the ice layer. Due to its low thermal conductivity and high albedo properties, snow acts as an efficient insulator and hence has a strong influence on the conductive heat flux. In the presence of snow, most of the incoming shortwave radiation is reflected and sent back to the atmosphere. The remaining shortwave radiation is attenuated further by the ice and in the ocean mixed layer [Gerland and Haas, 2011; Nicolaus *et al.*, 2010].

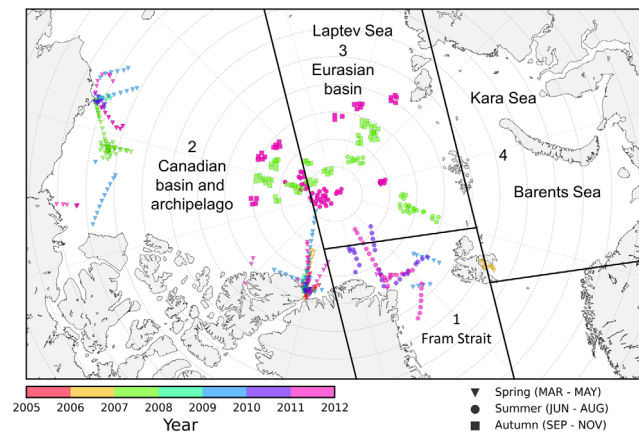


**Figure 2.** A map with the locations of all airborne EM sea-ice thickness surveys included in the ITDs. The color bar indicates the year in which the survey took place and the marker type indicates the season (inverted triangle: spring, circle: summer, and square: autumn). Black lines delimit different regions discussed in Table 3.

[10] Large-scale observations of snow thickness ( $h_s$ ) in the Arctic are rare. Warren *et al.* [1999] presented an Arctic snow depth climatology constructed from field measurements of the Soviet North Pole drifting stations for 1954–1991. During this time span, there was much more multi-year ice (MYI) in the Arctic than in recent years. Also, due

to the character of the observations on drifting ice, this climatology is limited only to snow measurements on top of level MYI.

[11] Previous studies from observations have demonstrated that  $h_s$  increases with the age of ice such as in Antarctica [Sturm and Massom, 2010]. However, various field observations did not show a direct correlation between the thickness of snow and ice [Eicken and Lange, 1989; Lange and Eicken, 1991; Sturm et al., 2002; Toyota et al., 2007]. Some empirical relationships between ice and snow thickness have been proposed for different ranges of  $h_i$ . For instance, Doronin [1971] retrieved  $h_s$  and  $h_i$  relations (i.e.,  $h_s = 0$  for  $h_i < 5$  cm;  $h_s = 0.05 h_i$  for  $5 \text{ cm} \leq h_i \leq 20$  cm and  $h_s = 0.1 h_i$  for  $h_i > 20$  cm) from satellite thermal imagery (AVHRR) data. This relationship was later reevaluated by Mäkynen et al. [2013]. The authors retrieved the relationship between  $h_i$  and  $h_s$  from the Soviet Union's airborne Server expeditions for late winter conditions between 1950 and 1989. The only difference to Doronin's relationships was observed when  $h_i > 20$  cm, where the slope was 10 % smaller ( $h_s = 0.09 h_i$  for  $h_i > 20$  cm) than the previous relationship for the same case. The empirical relationships between  $h_i$  and  $h_s$ , proposed by Mäkynen et al., were developed only for the Kara Sea and the eastern part of the Barents Sea and they strongly rely on atmospheric forcing data and its uncertainties particularly in air temperature and wind speed [Doronin, 1971; Mäkynen et al., 2013].

[12] In a recent work from NASA Operation IceBridge project,  $h_s$  is derived from airborne microwave snow radar measurements along transects of thousands of kilometers. Results from these observations suggest a higher snow accumulation of snow over MYI [Kurtz et al., 2012; Kwok et al., 2011]. However, the limited in situ measurements of snow on Arctic sea ice have demonstrated the heterogeneity in the distribution of snow thicknesses with respect to the geographical location as a consequence of environmental conditions such as humidity and wind causing erosion and further redistribution with accumulation in depressions and decrease in elevations [Forsström et al., 2011; Gerland and Haas, 2011; Haapala et al., 2013; Iacozza and Barber, 2010; Sturm et al., 2006].

[13] As a result, the correlation between ice and snow thicknesses based on Arctic snow observations is ambiguous. Hence, it is not plausible to generally expect a consistent deep snow layer over old ice, implied by long accumulation, and over rough surfaces; and a thin snow layer on top of young first year and level sea ice.

[14] Additionally, the complex physical processes acting over the snow layer (i.e., variable snow density in time and space, snow compaction due to wind effects, change in grain size due to age) are difficult to include in numerical models. Instead, simplified parameterizations are used [Hunke et al., 2010].

[15] In our model, snow accumulation is parameterized using precipitation and air temperature [Zhang et al., 1998]. The accumulated snow forms a layer of constant density on top of the ice. When enough snow is accumulated to submerge the surface of the ice, a simple flooding algorithm converts snow into ice until the ice-snow interface is lifted to sea level [Leppäranta, 1993]. Based on this model, we test here two different and simple methods of distributing the snow over the different thicknesses categories of the ice.

[16] In this work, we explore the sensitivity of the simulated sea-ice thickness to the treatment of snow and ice as sketched above. The paper is organized as follows: the model configuration is described in section 2.1, the sea-ice thickness distributions and snow depth parameterizations are introduced in section 2.1.1 and the heat flux calculations in section 2.1.2. Section 2.2 lists the sensitivity experiments of this work. Section 3 presents the results to the sensitivity of sea-ice thickness due to different ITDs (section 3.1) and to the different snow parameterizations (section 3.2). In section 3.3, we compare our results to the ICESat (Ice, Cloud, and land Elevation Satellite) sea-ice thickness derived from laser altimetry measurements. In section 3.4, we evaluate the resulting conductive heat flux and thermodynamic sea-ice growth. Finally, the discussion and conclusions are presented in sections 4 and 5.

## 2. Methods

### 2.1. Model Description and Setup

[17] We use the Massachusetts Institute of Technology general circulation model (MITgcm) [Marshall et al., 1997] in a regional coupled ocean-sea ice Arctic Ocean configuration similar to the configuration of NAOSIM (North Atlantic/Arctic Ocean Sea-Ice Model) [Karcher et al., 2011]. The domain covers the Arctic Ocean region, Nordic Seas and the North Atlantic down to approximately  $50^\circ\text{N}$  and has open boundaries in the North Atlantic and in the Pacific just south of Bering Strait. The horizontal resolution is  $1/4^\circ$  ( $\sim 28$  km) on a rotated grid with the grid equator passing through the North Pole. The vertical is discretized in 33 nonequally spaced levels with depths ranging from 10 m near the surface to approximately 356 m at maximum model depth of 4800 m. Vertical mixing in the ocean interior is achieved by a K-Profile Parameterization (KPP) scheme [Large et al., 1994] and tracers (temperature and salinity) are advected with an unconditionally stable seventh-order monotonicity preserving scheme [Darau and Tenaud, 2004] that requires no explicit diffusivity.

[18] The dynamic-thermodynamic sea-ice model of the MITgcm [Losch et al., 2010] uses a viscous-plastic rheology and a so-called zero-layer thermodynamics (i.e., zero heat capacity formulation) [Semtner, 1976] with a prescribed ITD [Hibler, 1979, 1980, 1984; Losch et al., 2010].

[19] The model is forced by realistic atmospheric conditions of the Coordinated Ocean Research Experiment (CORE) version 2 that are based on the reanalysis from the National Center for Atmospheric Research/National Centers for Environmental Prediction (NCAR/NCEP) [Large and Yeager, 2009]. This data set includes 6 hourly wind, atmospheric temperature and specific humidity, daily downward long and short-radiative fluxes and monthly precipitation fields. Surface salinity in ice free regions is restored to a mean salinity field (also CORE data) with a time scale of 180 days to suppress model drift. A monthly climatology of river runoff for the main Arctic rivers follows the AOMIP (Arctic Ocean Model Intercomparison Project) protocol based on Prange [2003].

[20] In the baseline configuration, the model is spun-up from the first day of January 1948 to the last day of December 1978. These 30 years of spin-up allow the model to adapt to the forcing. A control run using the baseline model

configuration and all subsequent sensitivity experiments start on 1 January 1979 and end on 31 December 2007 (29 years). The most important sea-ice parameters used in the model configuration are: ice strength ( $P^*$ ) of 27,000 Pa, a lead closing parameter ( $H_0$ ) of 0.5 m and surface albedos for ice and snow. Sea-ice and snow albedos are often tuned for realistic simulations of sea ice [Losch *et al.*, 2010]. In the baseline configuration the albedos are: 0.84 for dry snow, 0.70 for wet (melting) snow, 0.75 for dry ice, 0.66 for wet (melting) ice and 0.10 for open water, where the surface temperature of ice determines melting conditions.

### 2.1.1. Sea-Ice Thickness Distribution and Snow Depth Parameterizations

[21] In the sea-ice model of the baseline configuration (control), there are seven ice thickness categories between 0 and a maximum thickness of  $2h_i$  (twice the mean thickness  $h_i$ ) (see gray bars in Figures 1a and 1b). These seven thicknesses are given by  $h_{in} = h_i(2n - 1)/7$  and their distribution is flat, normalized and fixed in time [Hibler, 1984]. The bin width is constant with  $2h_i/7$ . All ITDs in Figure 1 are scaled for a mean thickness of 1 m.

[22] In order to add realism to this ad hoc ITD, we built two different ITDs from frequency distributions of total ice thicknesses (snow plus ice thickness) over level ice as measured by an airborne EM-bird in various locations of the Arctic Ocean. Figure 2 depicts the location of the flights that were used to construct the ITDs. Both ITDs have 15 ice categories, a maximum thickness of  $3h_i$  and a bin width of  $3h_i/15 = 0.2h_i$ . They differ in the amount of data that we used to construct them.

[23] For the first ITD (Figure 1a), we used a series of frequency distributions of sea-ice thickness obtained from 112 EM-bird flights of 19 field campaigns between 2005 and 2011. The data for this ITD are dominated by perennial MYI and averages over various ice types and seasons corresponding to Arctic summer, spring, and autumn. The area coverage of these flights includes various regions in the Arctic Ocean such as the western marginal seas in spring and the Transpolar Drift stream and Fram Strait in summer.

[24] For the second ITD (Figure 1b), we used the frequency distribution of sea-ice thickness from a single EM-bird campaign that was carried out during the *RV Polarstern* cruise ARK-XXVI/3 in 2011. This cruise took place during the sea-ice minimum in the central Arctic Ocean (August–October) (magenta squares and circles in Figure 2). The reasoning for choosing this single campaign is the small variation of the ice thickness distribution in the central Arctic Ocean, with the subsequent assumption that this ITD is a suitable description for homogenous sea-ice conditions including more first-year ice (FYI). Thus, this ITD represents the ongoing shift from MYI to younger first and second-year ice in the Arctic Ocean. By including this ITD in our model we aim to evaluate the response of modeled sea-ice thickness to this condition.

[25] The choice of ITD determines a factor in the loss term of ice concentration under melting conditions. In Hibler’s original ITD with equally distributed ice classes this factor is  $A/2h$  where  $A$  is the ice concentration and  $h$  the ice thickness:  $A/2h$ ,  $\delta h$  is the fractional area that is lost when the thickness of the thinnest ice class is reduced by  $\delta h$ . For the non-homogeneous distribution the factor  $1/2$  is

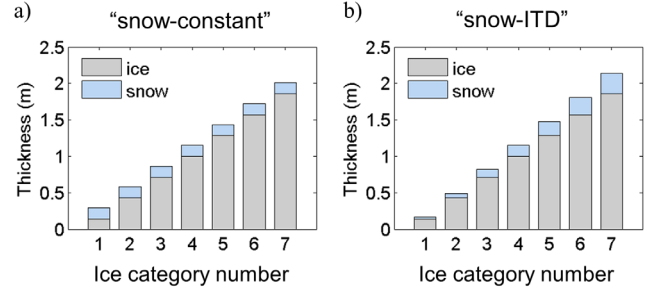


**Figure 3.** A schematic representation of the different snow parameterizations evaluated in this work: (a) “snow-constant,” the snow thickness is the same for all ice thickness categories and (b) “snow-ITD,” the snow has the same thickness distribution as the ice, so that the snow thickness is proportional to the ice thickness.

replaced by  $\frac{2 \sum_{k=1}^n (p_k k) - 1}{n}$ , where  $p_k$  is the distribution function and  $n$  the number of thickness classes. For the multi-campaign ITD this factor is 0.334 and for the single campaign ITD it is 0.336.

[26] Two different parameterizations for the redistribution of snow are used in this study: (1) snow depth is uniform and independent on the ice categories below, and (2) snow is distributed proportionally to the prescribed ITD. Our baseline model configuration follows the first type and will be hereinafter referred to as “snow-constant” (Figure 3a). The second parameterization will be referred to as “snow-ITD” (Figure 3b). Both parameterizations are an ad hoc solution in the absence of a clear understanding of the snow redistribution process, and neither form is unambiguously supported by observations (see above). By using these different snow distributions we attempt to estimate the uncertainties introduced by our limited knowledge about the snow distribution on the results of the sea-ice model.

### 2.1.2. Heat Flux Calculations and Thermodynamic Growth of Sea Ice

[27] We evaluate the thermodynamic growth of sea ice (melting and freezing rates) of our sensitivity experiments. The thermodynamic growth is determined from the conductive heat flux ( $F_c$  in  $\text{W m}^{-2}$ ) through the ice, in this case, through each of the 15 ice categories  $n$  in the realistic ITDs. The net growth includes a melting contribution from warm ocean water above freezing, but this is neglected in our presentation of the ice growth. The variability of the thermodynamic growth depends to a large extent on the ice and snow thicknesses. Thus,  $F_c$  is calculated according to equation (1) [Jeffries *et al.*, 1999]:

$$F_c = \frac{T_f - T_s}{\left(\frac{h_i}{K_i} + \frac{h_s}{K_s}\right)} \quad (1)$$

where  $T_f$  is the freezing point of seawater,  $T_s$  is the temperature at the surface of the snow,  $h_i$  and  $h_s$  are the mean sea-ice and snow thicknesses, and  $K_i$  and  $K_s$  are the sea-ice and snow thermal conductivities. For  $K_s$ , we use a value of  $0.31 \text{ W m}^{-1} \text{ K}^{-1}$  [Massom *et al.*, 1998] and for  $K_i$  we use  $2.16$

**Table 1.** Characteristics of the Simulations Subject to This Study

Simulation Number (Code Name)	Number of Categories in the Ice Thickness Distribution	Snow Parameterization
1 (control)	7 <sup>a</sup>	snow-constant
2 (snowITD_7)	7 <sup>a</sup>	snow-ITD
3 (snowc_15_1)	15 <sup>b</sup>	snow-constant
4 (snowc_15_19)	15 <sup>c</sup>	snow-constant
5 (snowITD_15_1)	15 <sup>b</sup>	snow-ITD
6 (snowITD_15_19)	15 <sup>c</sup>	snow-ITD

<sup>a</sup>Uniformly distributed.

<sup>b</sup>Obtained from one EM-bird campaign.

<sup>c</sup>Obtained from 19 EM-bird campaigns.

W m<sup>-1</sup> K<sup>-1</sup> [Cox and Weeks, 1988].  $F_c$  is defined as positive (upward) when the heat flux is directed from the ocean to the atmosphere through the ice/snow layer. Negative heat flux (downward heat flux warming the ocean) occurs when the temperature at the surface of the snow is higher than the freezing temperature of water at the bottom of the ice layer. The distribution of the thermodynamic growth is illustrated in section 3.4.

## 2.2. Model Simulations and Sensitivity Experiments

[28] We performed six simulation experiments (Table 1). Experiment 1 represents our control run and uses the baseline configuration of the MITgcm sea-ice model. Experiment 2 (snowITD\_7) provides insight into the effect of changing the snow parameterization to the second form (section 3.2). Experiments 3 and 4 (snowc\_15\_1 and snowc\_15\_19) evaluate the sensitivity of using two more realistic ITDs than the canonical homogeneous seven-ice categories (section 3.1) and allows also to study the sensitivity between the two realistic ITDs.

[29] Finally, a comparison between experiments 1 (control) with 5 (snowITD\_15\_1) and 6 (snowITD\_15\_19) describes the overall effect of combining different snow parameterizations and realistic ITDs (section 3.2). In all simulations, the model configuration (sea-ice and ocean parameters, as well as atmospheric forcing) and spin-up conditions are the same. The period from 1979 to 1989 is not analyzed to allow the model to adapt to the changes in the snow parameterization and ITD. Thus, the results presented here are based on monthly averages of the period 1990 to 2007 (18 years).

## 3. Results

[30] Most of the results presented in the following sections are spatial maps of climatologies, or differences

**Table 3.** The Annual Mean Sea-Ice Thickness for All Experiments and Divided Into Regions (See Figure 2) Over the Time Period (1990–2007) for DJF (December, January, and February), and SON (September, October, and November)

Experiment	1	2	3	4
	Fram Strait	Canadian Basin and Archipelago	Eurasian Basin	Kara and Barents Seas
<i>DJF</i>				
1 (control)	0.67	1.64	1.22	0.49
2 (snowITD_7)	1.05	2.36	1.80	0.63
3 (snowc_15_1)	0.71	1.59	1.20	0.48
4 (snowc_15_19)	0.76	1.73	1.27	0.49
5 (snowITD_15_1)	1.02	2.25	1.73	0.61
6 (snowITD_15_19)	1.15	2.57	1.97	0.67
<i>SON</i>				
1 (control)	0.69	1.13	0.59	0.22
2 (snowITD_7)	1.05	1.94	1.24	0.41
3 (snowc_15_1)	0.72	1.12	0.63	0.22
4 (snowc_15_19)	0.72	1.25	0.69	0.23
5 (snowITD_15_1)	1.02	1.83	1.20	0.40
6 (snowITD_15_19)	1.14	2.17	1.44	0.47

between climatologies, from 1990 to 2007. We show results of autumn (September–October–November) and winter (December–January–February) since most of the Arctic precipitation falls from August to October [Serreze and Maslanik, 1997]. The maximum snow accumulation is found during October, November and December in areas dominated by MYI [Sturm et al., 2002]. Further, autumn and winter are the only two seasons available in the satellite derived sea-ice thickness to which we compare our model results. The mean sea-ice thicknesses of each experiment averaged over the entire model domain are presented in Table 2.

[31] We divided the model domain into four subareas (Fram Strait, Canadian Basin and Archipelago, Eurasian Basin, and Barents and Kara Seas) (see Figure 2). The mean sea-ice thicknesses for each subarea are presented in Table 3.

### 3.1. Sensitivity of Simulated Sea-Ice Thickness to Different Ice Thickness Distributions

[32] First we discuss the shape of the different ITDs in Figure 1. For the actual simulations, the ITDs are rescaled to fit the modeled mean ice thickness in the grid cell. The Hibler [1984] ITD is flat and all ice thickness categories are equally frequent. The two observationally based ITDs have a similar shape: a mode at the thin ice categories and a tail toward the thicker ice categories. One of the differences between the ITDs is the location of the mode. The thickness mode in the ice distribution representing one

**Table 2.** The Annual and Seasonal Means and Their Standard Deviations of the Simulated Sea-Ice Thickness for All Experiments Averaged Over the Entire Model Domain Over the Time Period (1990–2007): DJF (December, January, and February), MAM (March, April, and May), JJA (June, July, and August), and SON (September, October, and November)

Experiment	Annual Mean	DJF	MAM	JJA	SON
1 (control)	1.27 ± 0.32	1.11 ± 0.33	1.49 ± 0.27	1.38 ± 0.42	0.76 ± 0.37
2 (snowITD_7)	1.78 ± 0.31	1.58 ± 0.38	2.01 ± 0.30	1.92 ± 0.44	1.33 ± 0.44
3 (snowc_15_1)	1.24 ± 0.30	1.09 ± 0.29	1.48 ± 0.23	1.38 ± 0.38	0.77 ± 0.30
4 (snowc_15_19)	1.32 ± 0.30	1.17 ± 0.30	1.56 ± 0.25	1.46 ± 0.39	0.85 ± 0.32
5 (snowITD_15_1)	1.69 ± 0.31	1.51 ± 0.36	1.93 ± 0.29	1.84 ± 0.43	1.27 ± 0.39
6 (snowITD_15_19)	1.89 ± 0.32	1.71 ± 0.39	2.13 ± 0.32	2.05 ± 0.46	1.49 ± 0.43

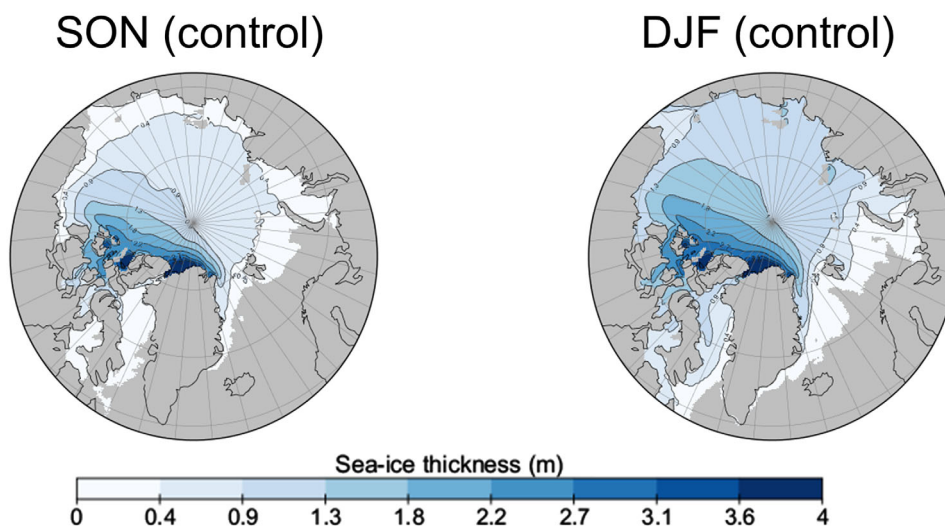


**Figure 4.** The spatial distribution of the sea-ice thickness in the control run for autumn (SON) and winter (DJF).

single campaign (Figure 1b) corresponds to category 4, with a range of thickness between 0.6 and 0.8 m. Category 4 is closely followed by category 5, with a range of thickness between 0.8 and 1.0 m. The ice thickness mode in the multicampaign ITD (Figure 1a) corresponds to category 3, with a range of thickness between 0.4 and 0.6 m. In addition, in the multicampaign ITD the frequency between the mode and the following thicker category is contrastingly large compared to this difference in the single-campaign ITD. More important for the resulting sea-ice thickness is the distribution of the thinnest ice categories. These play a fundamental role in setting the freezing and melting sea-ice rates. In the single-campaign ITD, the four thinner ice categories are less frequent than in the multicampaign ITD.

[33] In the control run, the sea-ice thickness is largely underestimated in almost the entire Arctic Ocean when compared to remote-sensed estimates (see section 3.3). In this baseline configuration, thin ice ( $<1$  m) dominates in regions such as the Eurasian Basin and Fram Strait, where according to remote-sensed estimations, thicker ice ( $>1$  m) is expected to be found (Figure 4 and values per areas in Table 3). In regions with MYI (i.e., Lincoln Sea, Canadian Arctic Archipelago), the modeled sea-ice thickness is underestimated by about 2 m compared to ICESat. The sea-ice extent, however, agrees with the satellite data (not shown). The simulated Arctic-wide mean sea-ice thickness over the analyzed period (1990–2007) is almost unchanged in all seasons after replacing the 7-category ITD with the 15-category ITDs. The differences are below 0.1 m (experiment 1 (control), 3 (snowc\_15\_1), and 4 (snowc\_15\_19) in Table 2). The largest differences (0.09 m) are found with the multicampaign ITD in the Canadian Basin and Canadian Arctic Archipelago region during winter (Table 3).

[34] On a spatial map, the differences between experiments 1 (control) and 3 (snowc\_15\_1) are negligible except near the coast of Northern Greenland in the Canadian Arctic Archipelago, and west of Svalbard (Figures 5a and 5b). In the Canadian Basin, the changes between experiments 1 (control) and 4 (snowc\_15\_19) are larger than between experiments 1 and 3 (Figures 5c and 5d). However, the differences between experiments 3 and 4 are similar for

autumn and winter (Figures 5e and 5f). We attribute this to the fact that the thinnest ice categories are more frequent in the multicampaign ITD of experiment 4 than in the single flight ITD (Figure 1).

### 3.2. Sensitivity of Simulated Sea-Ice Thickness Due to Snow Parameterizations

[35] The sensitivity to different snow parameterizations is much larger than the sensitivity to different ITDs. When the snow parameterization is changed to the snow-ITD parameterization in the baseline model configuration (experiment 2) the Arctic-wide mean sea-ice thickness increases by about 0.5 m (column 2, Table 2), whereas the mean snow depth is almost unchanged (0.13 m with snow-constant and 0.12 m with snow-ITD) (not shown). Similar results are obtained also for both 15-categories ITDs and for all seasons (Table 2).

[36] Figure 6 depicts the difference in sea-ice thickness due to the different snow parameterizations for all three ITDs. The largest differences with respect to the snow parameterization are obtained in all seasons with the multicampaign ITD (Figures 6c and 6d) while the differences are slightly smaller for the original 7-categories ITD (Figures 6a and 6b). The single-campaign ITD (Figures 6e and 6f) leads to the smallest sensitivity to the snow parameterization. The differences are largest in the Canadian Basin and Canadian Archipelago in autumn and winter (from 0.7 to 0.9 m depending on the ITD) and lowest in the Kara and Barents Seas (0.1 m in winter and from 0.2 to 0.3 m in autumn). Typical changes are about 0.3 m in the Fram Strait and about 0.5 m in the Eurasian Basin (Table 3).

### 3.3. Comparison to Laser Altimetry-Derived Sea-Ice Thickness

[37] To evaluate our model simulations, we compare the simulated sea-ice thickness to ice thickness maps based on laser altimetry measurements (ICESat) [Zwally *et al.*, 2002]. These data are available for February/March (winter) and October/November (autumn) from 2003 to 2008. The ICESat thickness measurements are known to overestimate thin ice ( $<1$  m) due to the large uncertainty of  $\sim 0.7$

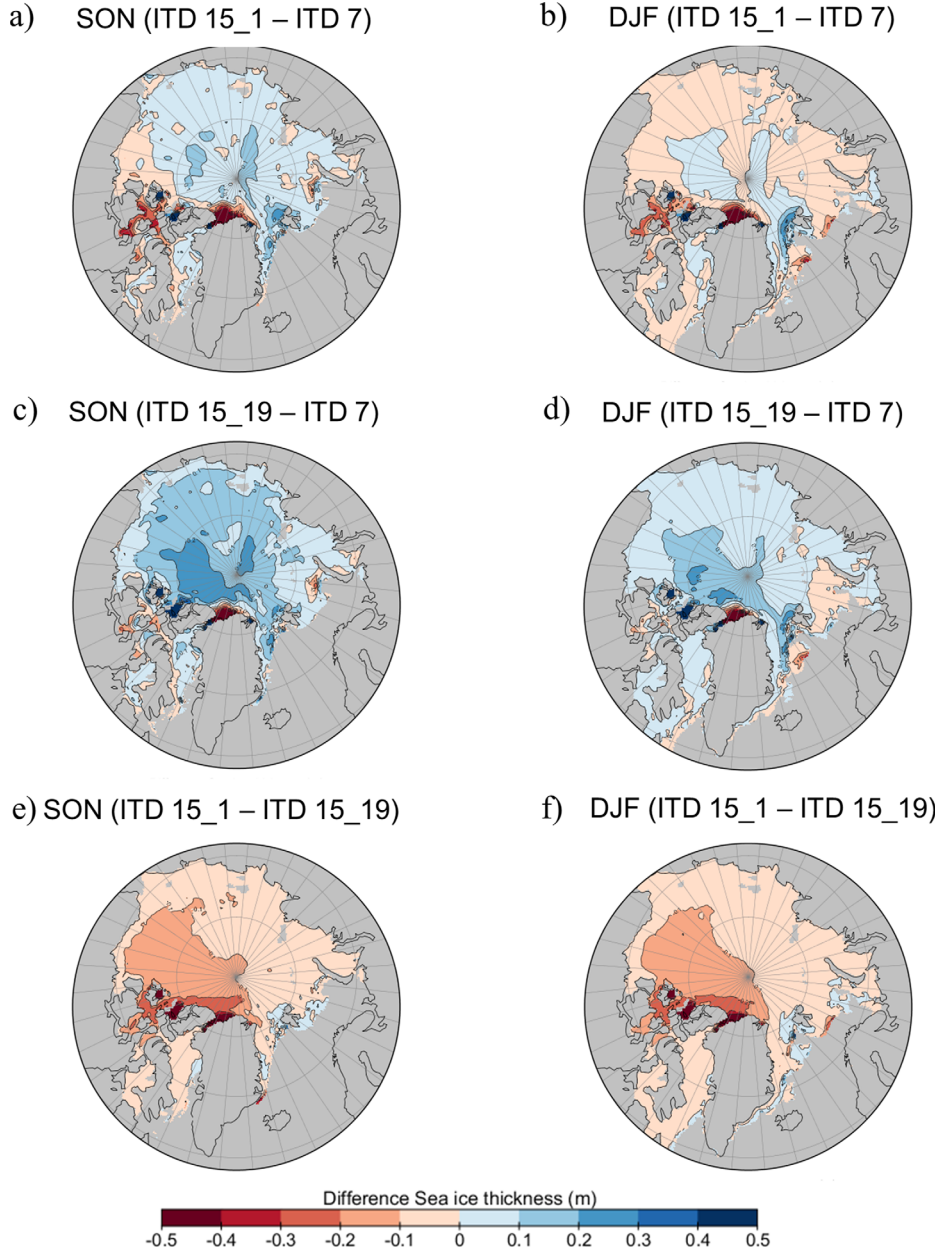


**Figure 5.** Spatial distribution of difference in sea-ice thickness (m) for: experiment 3 minus experiment 1 (snowc\_15\_1–control) during (a) autumn (SON) and (b) winter (DJF); experiment 4 minus experiment 1 (snowc\_15\_19–control) during (c) autumn and (d) winter; and experiment 3 minus experiment 4 (snowc\_15\_1–snowc\_15\_19) during (e) autumn and (f) winter. The results are integrated from 1990 to 2007.

m in the ice thickness estimates (within a 25 km segment) [Kwok and Cunningham, 2008]. Therefore, the data are only available in the inner Arctic. The March/April 2007 (Figure 7a) and October/November 2007 (Figure 7d) ICESat thicknesses are shown together with the corresponding simulated ice thicknesses of the control run (Figures 7b and 7e) and experiment 6 (snowITD\_15\_19) (Figures 7c and 7f). In order to quantify the differences in sea-ice thickness between model and satellite-derived data, we limited the area coverage of the modeled sea ice to the area coverage in the ICESat product. For all measurement periods the simulated ice thickness from the experiments with the snow-ITD parameterization are much closer to the ICESat data than the simulations with the snow-constant parame-

terization. The differences in winter are relatively small (0.1 m), but in autumn even the largest simulated ice thicknesses are well below the ICESat estimates (Figure 8). We attribute the differences in autumn to the overestimation of thin ice in the ICESat data product because we observe that in regions where there is no presence of ice or it is very thin, in the simulations there is implausibly thick ice of about 1 m in the ICESat fields (see Figures 7d–7f).

### 3.4. Conductive Heat Flux and Thermodynamic Growth of Sea Ice

[38] We evaluate the conductive heat flux contribution ( $F_c$ ) through the snow and ice layer for each of the 15 ice categories of the ITDs in experiments 3–6. The total  $F_c$  in a

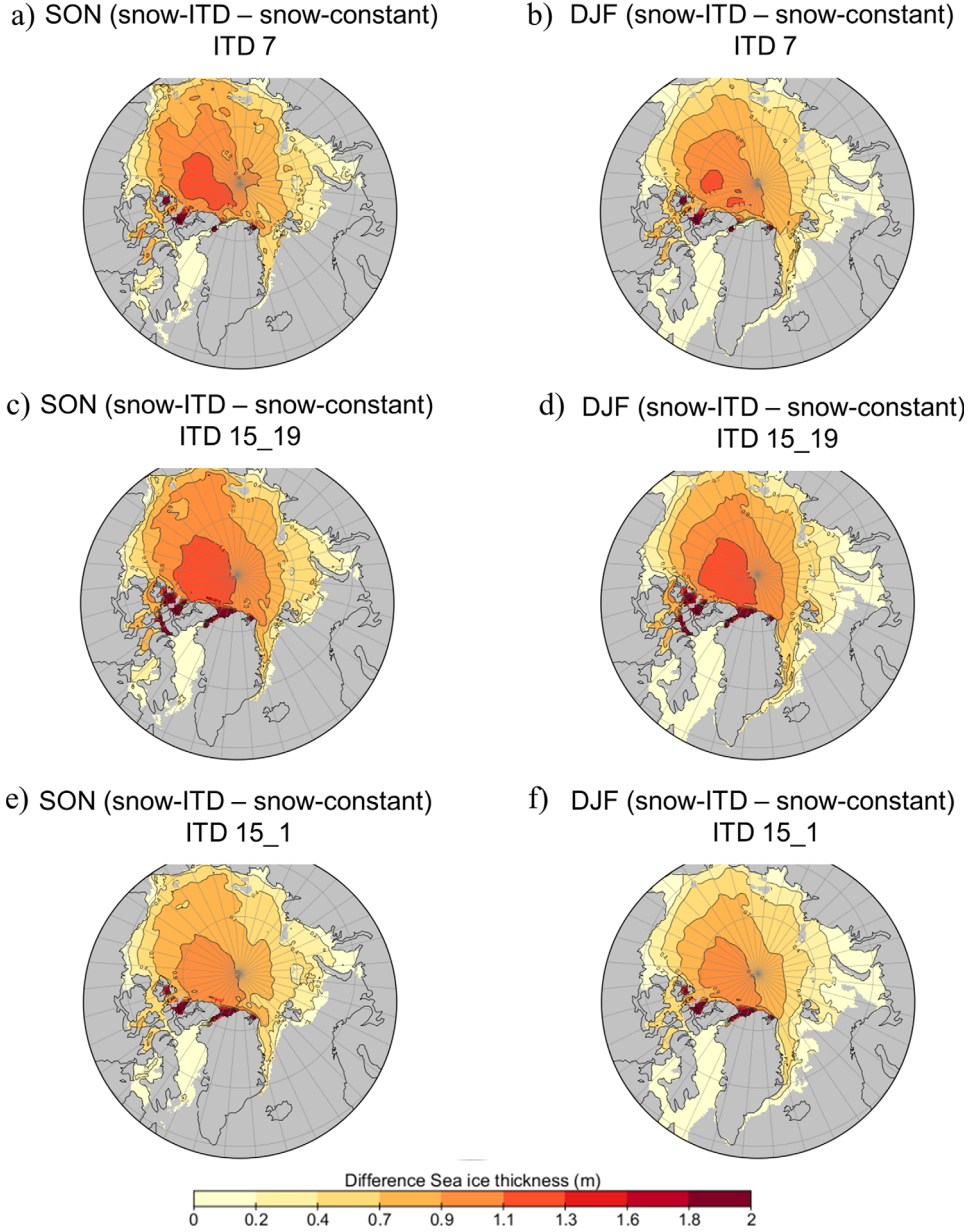


**Figure 6.** Spatial distribution of difference in sea-ice thickness (m) with different snow parameterizations for winter (DJF) and autumn (SON): (a and b) experiment 2–experiment 1 (snowITD\_7–control); (c and d) experiment 6–experiment 4 (snowITD\_15\_19 – snowc\_15\_19), and (e and f) experiment 5–experiment 3 (snowITD\_15\_1–snowc\_15\_1). The results are integrated from 1990 to 2007.

grid cell is the sum of the flux through each individual ice category.

[39] In Figure 9, we show an example of the conductive heat flux in each ice category for winter in a single model grid cell located near the North Pole (see inset map in Figure 9) where sea-ice cover is present throughout the year.

[40] In the experiments with snow-constant (3 and 4), the shape of the  $F_c$  over the ice categories is similar to the shape of the ITDs (i.e., higher  $F_c$  through the ice categories that are more frequent) while in the experiments with snow-ITD (5 and 6) the lowest ice categories are amplified because here thinner snow allows more heat flux.

[41] Toward the thicker ice and less frequent ice categories, the  $F_c$  decreases toward zero in all experiments

because the ice is too thick to allow any significant flux (Figure 9).

[42] A clear distinction between the experiments with and without snow-constant distribution (experiments 3 and 4 versus experiments 5 and 6) is visible for the first ice category. In the experiments with snow-ITD (5 and 6), the  $F_c$  values are about three times higher than for the experiments with snow-constant (3 and 4) due to the presence of lower snow thickness using the snow-ITD (Figure 9).

[43] Furthermore, we evaluate the effect of the different parameterizations on the Arctic-wide melting and freezing rates of the sea ice. We calculated the monthly mean thermodynamic growth of ice. In Figure 10a, the annual cycle of the thermodynamic growth for the control run is shown. In

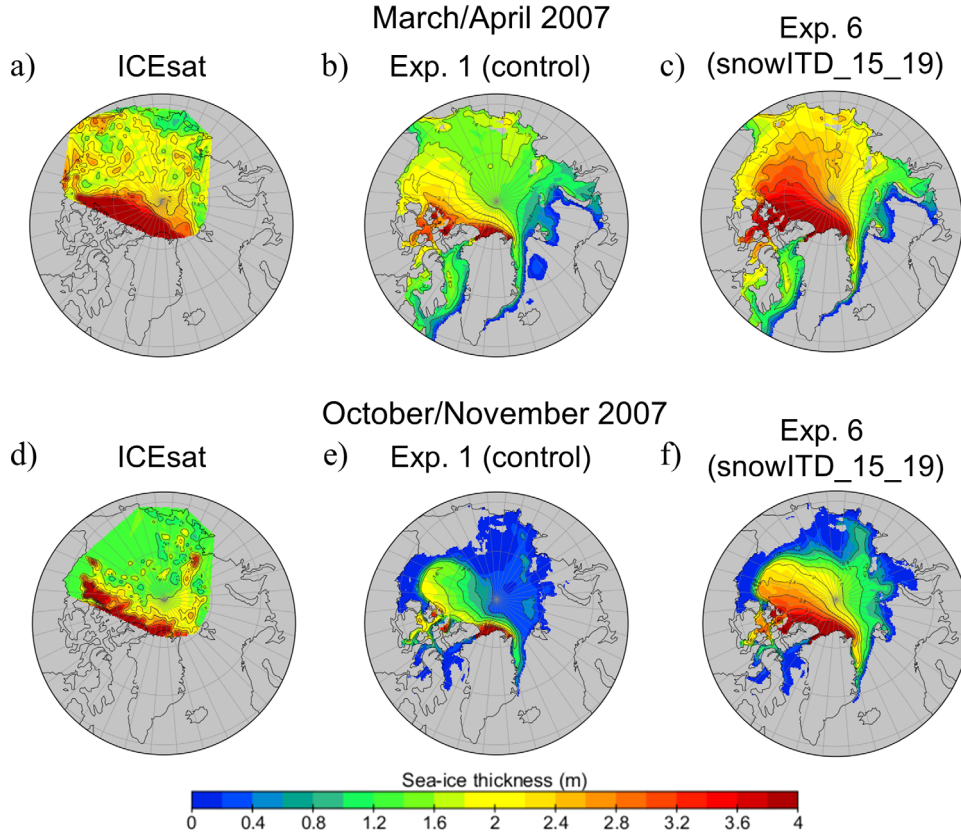


**Figure 7.** Comparison of sea-ice thickness (m) from the model and from laser altimetry satellite. Data from (a and d) ICESat, (b and e) experiment 1 (control), and (c and f) experiment 6 (snowITD\_15\_19), (top) for March/April 2007 and (bottom) October/November 2007.

the months between October to April, freezing dominates with the highest freezing rate in December ( $1490 \text{ km}^3 \text{ month}^{-1}$ ). Melting dominates from May to September, with the highest melting rate in July ( $-3591 \text{ km}^3 \text{ month}^{-1}$ ).

[44] The effects of the different parameterizations on the ice growth are illustrated by plotting the difference of the net growth in the five sensitivity experiments and the control run (Figure 10b). The sea-ice growth increases by

about  $150 \text{ km}^3 \text{ month}^{-1}$  from October to May over the control run with seven ice categories (experiment 1) when an ITD with 15 categories is used (experiments 3 and 4). In these experiments, the melting rate also increases by about  $60 \text{ km}^3 \text{ month}^{-1}$  from June to September. Both effects can be explained by a larger fraction of thin ice in the realistic ITD with 15 categories: thin ice allows more conductive

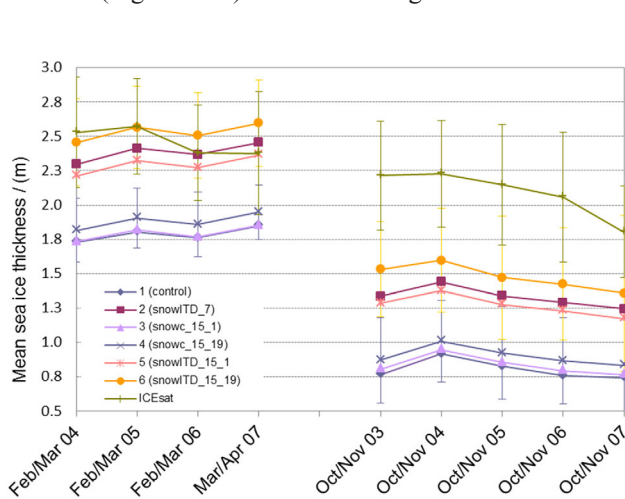


**Figure 8.** Average sea-ice thickness for the months and years (x axis) from the experiment simulations and from ICESat data. Error bars represent  $\pm 1\sigma$  from the mean.

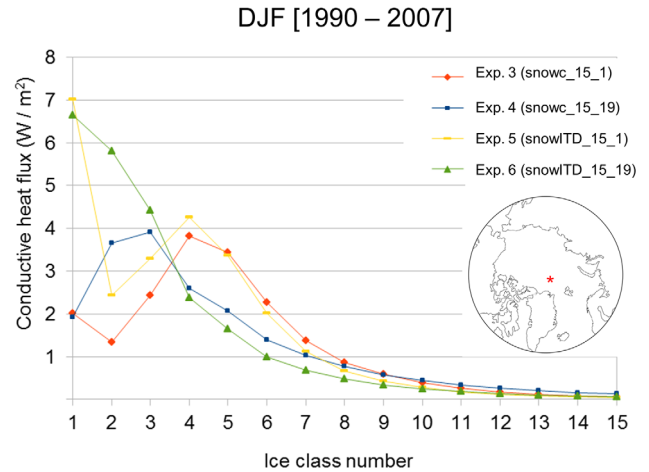


**Figure 9.** Mean conductive heat flux ( $F_c$  in  $\text{W m}^{-2}$ ) through the ice-covered region in a model grid cell (star in inset map) for the 15 ice categories in experiments 3–6 during winter months (December–January–February) for 1990–2007.

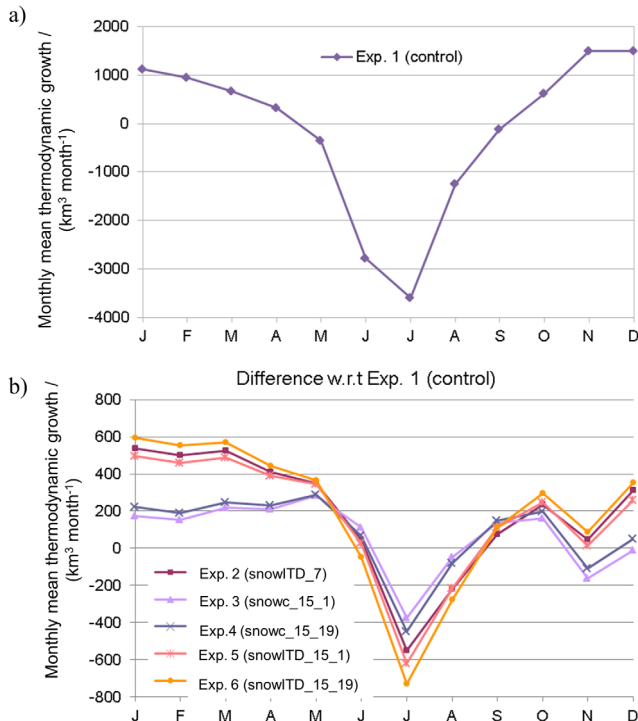


**Figure 10.** (a) Annual thermodynamic growth ( $\text{km}^3 \text{ month}^{-1}$ ) of simulated Arctic sea ice integrated over the period of analysis for the control run used as reference; (b) Difference between further experiments minus the control run. Positive values indicate sea-ice freezing and negative values indicate sea-ice melting.

heat flux (see equation (1)) and thus more freezing and melting. The net effect is thicker ice because the influence is larger for the freezing period, but the comparatively large fraction of thin ice always allows ice growth and freezing.

[45] A general clustering of experiments with and without snow-constant is visible in Figure 10b. Larger freezing and melting rates occur in experiment 6 (snowITD\_15\_19) closely followed by experiment 5 (snowITD\_15\_1), and experiment 2 (snowITD\_7). In the latter, we observe the second largest freezing rate and the third largest melting rates. A second cluster of experiments is formed by experiments 3 and 4, both with snow-constant.

[46] As expected, the combined effect of a more realistic ITD and a snow-ITD parameterization leads to a higher sea-ice growth rate (Figure 10b). We calculated the difference in thermodynamic sea-ice growth between experiments 5 and 6 minus experiment 1 (control). A mean sea-ice growth of  $180 \text{ km}^3 \text{ month}^{-1}$  was observed throughout the year, with a mean from December to May of  $443 \text{ km}^3 \text{ month}^{-1}$  and a mean from April to November of  $-82 \text{ km}^3 \text{ month}^{-1}$ . The largest difference was found in January ( $545 \text{ km}^3 \text{ month}^{-1}$ ) and the lowest during June to August (mean of  $-310 \text{ km}^3 \text{ month}^{-1}$ ) when the melt rates are generally larger than in the baseline experiment (Figure 10b).

#### 4. Discussion

[47] The mean sea-ice thickness in each model grid cell is the convolution of the thickness in each category with

the distribution  $h_i = \sum_{k=1}^n (p_k h_{ik})$ . To explore the impact of an

ITD in our model configuration, we prescribed two nonhomogeneous ITDs based on sea-ice thickness that was retrieved from airborne measurements and we evaluate the resulting simulated sea-ice thickness. In general, our main result is a considerable increase in the simulated sea-ice thickness with an ITD of higher number of ice categories compared to the original model by *Hibler* [1984].

[48] We find, however, a high sensitivity to the details of the two 15-categories ITDs. They differ in the distribution of the thinner thicknesses, particularly in the location of the modes. The position of the modes of thin ice is expected to be important for energy exchange since the representation of the thinnest ice is directly related to the thermodynamic growth of ice.

[49] Compared to the ITD based on a single campaign, thin ice is more frequent in the multicampaign ITD. As a result, the simulated sea ice is thicker than using the single-campaign ITD. In addition, there is more MYI due to the inclusion of data collected during spring, and this is reflected in the presence of more thick-ice categories than for the single-campaign ITD. In contrast, in the single-campaign ITD the mode is located in a slightly thicker ice type and the frequency difference to the next ice category is comparably low. The single-campaign ITD represents the minimum sea-ice extent observed at the end of the melt season in 2011, thus the sea ice during the sampling period was dominated by melting first-year ice.

[50] The availability of EM-bird data provides a great opportunity to include realistic and present sea-ice thickness measurements in sea-ice modeling. However, due to different logistics during the sampling with the EM-bird in spring (land-based surveys) and summer (ship-based surveys), the data are biased toward MYI in spring and toward FYI in summer. This means that the majority of FYI is in the melting state and there is less thin ice in the scaled ITDs than the sum of all data, which scales typical FYI thicknesses to thin ice due to the larger ratio of mean to modal ice thickness of MYI.

[51] Most of the data available from observations were collected during Arctic spring, summer, and autumn. The absence of winter data (December–February) can lead to a misrepresentation of the sea-ice thickness during this season in the shape of the ITD. However, we can assume that the general shape of a winter ITD is not fundamentally different to that measured in spring because ice formation and deformation likely have shaped a typical winter ITD already in late autumn. Thus, the actual ITD shape in a specific region in spring depends mainly on the ice formation and deformation history throughout winter.

[52] Currently, observations of sea-ice thickness from field measurements, such as the ones from airborne EM-bird measurements, are a valuable source of data to generate an ITD for the Arctic region with potential application in sea-ice models. However, the use of a fixed ITD in global climate models from observations of the past decade must be done with caution due to the lack of representation of the presently fast changing conditions on the Arctic sea ice. It is also important noting that due to the nature of the EM-bird measurements, the retrieved ice thickness

represents the snow and ice layer for level ice. Furthermore, thick ice in the form of ridges is not well constrained by this method and is underestimated due to footprint smoothing.

[53] Besides the details of the ice thickness distributions, our results show an even larger sensitivity of sea-ice thickness, and melting rates, to the distribution of snow on top of the individual ice categories. This change in the model configuration leads to ice thicknesses that are closer to ICE-Sat values. With a nonuniform snow-ITD, a mean increase of 0.56 m sea-ice thickness in the entire model domain and about 1 m in the Canadian Basin and Canadian Arctic Archipelago were found compared to using a snow-constant distribution. The larger increase in sea-ice thickness in certain regions of the model domain does not seem to be related to the amount of the sea-ice thickness data available to construct the ITDs (i.e., more observations available, larger sea-ice thickness increase), but rather to the type of ice (i.e., MYI or FYI). Thus, where there is normally thicker ice, a larger increase in thickness is found with a snow-ITD distribution.

[54] Furthermore, the sensitivity of the snow distribution on sea-ice thickness can be increased, or reduced, by the selection of the ITD. We observe a higher sensitivity to the snow parameterization for a multicampaign ITD compared to a single-campaign ITD. This is possibly due to the different accumulation of snow relative to the different ice categories.

[55] These results are corroborated by the melting and freezing rates of sea ice, where we observe more sea-ice growth during the freezing months when a snow-ITD is used. This effect is more pronounced for the more realistic 15-category ITDs. However, the larger freezing rates go along with larger melt rates during summer. This effect is probably caused by more thin ice in the observation-based ITDs allowing more heat flux and ocean warming during summer, which in turn leads to higher melt rates.

[56] We compared our modeled thermodynamic growth to observed values reported by *Serreze et al.* [2007a] who estimated growth from net surface heat flux from ERA-40 data (1979–2001), hydrographic data for ocean sensible heat storage, and observations of the latent heat content of the ice divergence term. This was done over an Arctic Ocean domain similar to our model domain. For September, *Serreze et al.* report ice growth of 6 cm; we obtained for the same month a lower value for the mean model thermodynamic growth of  $100 \text{ km}^3$  (or 1.8 cm) in the control run; and a value of  $500 \text{ km}^3$  (or 9 cm for a mean sea-ice area of  $5.5 \times 10^6 \text{ km}^2$ ) for the parameterization with snow-ITD, which is an ice growth 50 % bigger than the *Serreze et al.* value. For February, we obtained a mean thermodynamic growth of  $1200 \text{ km}^3$ , that is an ice growth of 9 cm in the control run, and up to 16 cm (for a mean sea-ice area of  $11 \times 10^6 \text{ km}^2$ ) in our parameterization of experiment 6 (snowITD\_15\_19). These values are both lower than the values reported by *Serreze et al.* of 24 cm. The differences between these comparisons may also fall within the uncertainties in the estimates (e.g., errors in the reanalysis data). Our conductive heat flux calculations per ice category confirm the important role of a better description of the snow layer. In the experiments with snow-constant a thicker layer of snow is accumulated on top of thin ice, generating more

insulation with a decrease in  $F_c$  and a resulting low ice thickness during winter. In contrast, the experiments with snow-ITD have a thinner snow layer on top of thin ice, allowing a higher  $F_c$  through the snow and ice layer and a clear increase in sea-ice thickness. Because most of the Arctic sea ice is currently dominated by first-year ice (between 0.3 and 2 m), a prescribed ITD with better resolved thin ice, will also lead to a higher sensitivity when a snow-ITD is prescribed.

[57] We cannot suggest a best candidate for future simulations in numerical studies since both parameterizations have advantages and disadvantages from a physical point of view. A snow layer with a constant distribution can lead to too much snow accumulation on a thin ice layer and, as a consequence be inconsistent with the flooding algorithm that acts on the mean ice and snow layers. On the other hand, there is little observational evidence to suggest that the depth of the snow layer is proportional to the depth of the underlying sea ice.

[58] By introducing a different snow parameterization and distributing it according to the prescribed ITD, we observe a clear improvement in the modeled sea-ice thickness toward the satellite data during winter months. However, even with this snow parameterization the model simulations do not compare well with ICESat data in autumn (October/November). We attribute this bias to the fact that ICESat data does not properly represent thin ice ( $<1 \text{ m}$ ) which is present in autumn in large areas. The zero heat capacity approximation in the modeled sea ice, however, can also be a factor that contributes to this difference.

## 5. Conclusions

[59] Our results provide insight on the high sensitivity that simulated Arctic sea-ice thickness pose to different snow parameterizations and different descriptions of an ice thickness distribution. These parameterizations play an important role in optimizing simulated sea-ice cover; an appropriate choice can improve the representation of its energy and mass balance. Prescribing a better resolved ITD derived from field observations leads only to a moderate increase of simulated sea-ice thickness, but the sensitivity of ice properties to the snow parameterizations has a larger impact: simulated sea ice is much thicker when the snow is distributed according to the ITD (snow-ITD), especially when is combined with a realistic ITD with more categories.

[60] Whenever the price for a dynamic ITD is too high, we suggest that a more realistic distribution of sea-ice thickness obtained from field observations be prescribed for a better description on the current state of the Arctic sea ice. The treatment of the snow distribution is clearly important for the simulated ice thickness, but the details of such parameterization are still uncertain. Today, many observations of combined snow and ice thicknesses are available to help further development of snow parameterizations, but we encourage even more field observations at large scales in order to find a representative and robust statistical relation between snow and sea ice. This relation will improve the current parameterizations in models contributing to the reduction of uncertainties. This will also help to constrain the redistribution processes in dynamic ITD models;

eventually, realistic ITDs in sea-ice models are an important aspect toward representing the fast changes occurring presently in the Arctic Ocean and improving future projections.

[61] **Acknowledgments.** This work was possible thanks to the financial support of the European Commission as part of the project ArcRisk (Arctic Health Risks: Impacts on health in the Arctic and Europe owing to climate-induced changes in contaminant cycling) (FP7 GA226534), and by the BMBF (Federal Ministry of Education and Research, Germany) as part of the Joint Research Project ERANET EUROPOLAR—SATICE (Arctic Ocean sea-ice and ocean circulation changes using satellite methods) (03F0615A) of the European Science Foundation.

## References

- Cox, G. F. N., and W. F. Weeks (1988), Numerical simulations of the profile properties of undeformed first-year ice during the growth season, *J. Geophys. Res.*, *93*, 12,449–12,469, doi:10.1029/JC093iC10p12449.
- Daru, V., and C. Tenaud (2004), High order one-step monotonicity preserving schemes for unsteady flow calculations, *J. Comput. Phys.*, *193*, 563–594, doi:10.1016/j.jcp.2003.08.023.
- Doronin, Y. (1971), *Thermal Interaction of the Atmosphere and the Hydrosphere in the Arctic*, Isr. Prog. for Sci. Trans., Jerusalem.
- Eicken, H., and M. A. Lange (1989), Development and properties of sea ice in the coastal regime of the southeastern Weddell Sea, *J. Geophys. Res.*, *94*, 8193–8206, doi:10.1029/JC094iC06p08193.
- Forsström, S., S. Gerland, and C. A. Pedersen (2011), Thickness and density of snow-covered sea ice and hydrostatic equilibrium assumption from in situ measurements in Fram Strait, the Barents Sea and the Svalbard coast, *Ann. Glaciol.*, *52*(57), 261–270, doi:10.3189/172756411795931598.
- Gerland, S., and C. Haas (2011), Snow-depth observations by adventurers traveling on Arctic sea ice, *Ann. Glaciol.*, *52*(57), 369–376, doi:10.3189/172756411795931552.
- Haapala, J., M. Lensu, M. Dumont, A. H. H. Renner, M. A. Granskog, and S. Gerland (2013), Small-scale horizontal variability of snow, sea-ice thickness and freeboard in the first-year ice region north of Svalbard, *Ann. Glaciol.*, *54*(62), 261–266, doi:10.3189/2013AoG62A157.
- Haas, C., S. Hendricks, H. Eicken, and A. Herber (2010), Synoptic airborne thickness surveys reveal state of Arctic sea ice cover, *Geophys. Res. Lett.*, *37*, L09501, doi:10.1029/2010GL042652.
- Hibler, W. D. (1979), A dynamic thermodynamic sea ice model, *J. Phys. Oceanogr.*, *9*, 815–846, doi:10.1175/1520-0485(1979)009<0815:ADT-SIM>2.0.CO;2.
- Hibler, W. D. (1980), Modeling a variable thickness sea ice cover, *Mon. Weather Rev.*, *108*, 1943–1973, doi:10.1175/1520-0493(1980)108<1943:MAVTSI>2.0.CO;2.
- Hibler, W. D. (1984), The role of sea ice dynamics in modelling CO<sub>2</sub> increases, in *Climate Processes and Climate Sensitivity*, edited by J. E. Hansen, and T. Takahashi, pp. 238–253, AGU, Washington, D. C.
- Hunke, E. C., and C. M. Bitz (2009), Age characteristics in a multidecadal Arctic sea ice simulation, *J. Geophys. Res.*, *114*, C08013, doi:10.1029/2008JC005186.
- Hunke, E. C., H. Lipscomb, and A. K. Turner (2010), Sea-ice models for climate study: Retrospective and new directions, *J. Glaciol.*, *56*(200), 1162–1172, doi:10.3189/002214311796406095.
- Iacozza, J., and D. G. Barber (2010), An examination of snow redistribution over smooth land-fast sea ice, *Hydrol. Processes*, *24*, 850–865, doi:10.1002/hyp.7526.
- Jeffries, M. O., J. Zhang, K. Frey, and N. Kozlenko (1999), Estimating late winter heat flow to the atmosphere from the lake-dominated Alaskan North Slope, *J. Glaciol.*, *45*, 315–324, doi:10.3189/00221439979377095.
- Karcher, M., A. Beszczynska-Moeller, F. Kauker, R. Gerdes, S. Heyden, B. Rudels, and U. Schauer (2011), Arctic Ocean warming and its consequences for the Denmark Strait overflow, *J. Geophys. Res.*, *116*, C02037, doi:10.1029/2010JC006265.
- Kreyscher, M., M. Harder, P. Lemke, and G. M. Flato (2000), Results of the sea-ice model intercomparison project: Evaluation of sea ice rheology schemes for use in climate simulations, *J. Geophys. Res.*, *105*, 11,299–11,320, doi:10.1029/1999JC000016.
- Kurtz, N. T., S. L. Farrell, M. Studinger, N. Galin, J. P. Harbeck, R. Lindsay, V. D. Onana, B. Panzer, and S. Sonntag (2012), Sea ice thickness, freeboard, and snow depth products from Operation IceBridge airborne data, *Cryosphere Discuss.*, *6*, 4771–4827, doi:10.5194/tcd-6-4771-2012.
- Kwok, R., and G. F. Cunningham (2008), ICESat over Arctic sea ice: Estimation of snow depth and ice thickness, *J. Geophys. Res.*, *113*, C08010, doi:10.1029/2008JC004753.
- Kwok, R., B. Panzer, C. Leuschen, S. Pang, T. Markus, B. Holt, and S. Gogineni (2011), Airborne surveys of snow depth over Arctic sea ice, *J. Geophys. Res.*, *116*, C11018, doi:10.1029/2011JC007371.
- Lange, M. A., and H. Eicken (1991), The sea ice thickness distribution in the northwestern Weddell Sea, *J. Geophys. Res.*, *96*, 4821–4837, doi:10.1029/90JC02441.
- Large, W. G., and S. G. Yeager (2009), The global climatology of an inter-annually varying air-sea flux data set, *Clim. Dyn.*, *33*, 341–364, doi:10.1007/s00382-008-0441-3.
- Large, W. G., J. C. McWilliams, and S. C. Doney (1994), Oceanic vertical mixing: A review and a model with a nonlocal boundary layer parameterization, *Rev. Geophys.*, *32*, 363–403, doi:10.1029/94RG01872.
- Leppäranta, M. (1993), A growth model for black ice, snow ice and snow thickness in subarctic basins, *Nordic Hydrol.*, *14*, 59–70, doi:10.2166/nh.1983.006.
- Losch, M., D. Menemenlis, J.-M. Campin, P. Heimbach, and C. Hill (2010), On the formulation of sea-ice models: Part 1: Effects of different solver implementations and parameterizations, *Ocean Modell.*, *33*(1–2), 129–144, doi:10.1016/j.ocemod.2009.12.008.
- Mäkynen, M., B. Cheng, and M. Similä (2013), On the accuracy of thin-ice thickness retrieval using MODIS thermal imagery over Arctic first-year ice, *Ann. Glaciol.*, *54*(62), 87–96, doi:10.3189/2013AoG62A166.
- Marshall, J., A. J. Adcroft, C. N. Hill, L. Perelman, and C. Heisey (1997), A finite-volume, incompressible Navier Stokes model for studies of the ocean on parallel computers, *J. Geophys. Res.*, *102*, 5753–5766, doi:10.1029/96JC02775.
- Massom, R. A., V. I. Lytle, A. P. Worby, and I. Allison (1998), Winter snow cover variability on East Arctic sea ice, *J. Geophys. Res.*, *103*, 24,837–24,855, doi:10.1029/98JC01617.
- Nicolaus, M., S. Gerland, S. R. Hudson, S. Hanson, J. Haapala, and D. K. Perovich (2010), Seasonality of spectral albedo and transmittance as observed in the Arctic Transpolar Drift in 2007, *J. Geophys. Res.*, *115*, C11011, doi:10.1029/2009JC006074.
- Prange, M. (2003), Einfluss arktischer Süßwasserquellen auf die Zirkulation im Nordmeer und im Nordatlantik in einem prognostischen Ozean-Meereis-Modell, *Rep. Polar Mar. Res.* *468*, p. 220. Alfred Wegener Inst., Bremerhaven, Germany.
- Semtner, A. J. (1976), A model for the thermodynamic growth of sea ice in numerical investigations of climate, *J. Phys. Oceanogr.*, *6*, 379–389, doi:10.1175/1520-0485(1976)006<0379:AMFTTG>2.0.CO;2.
- Serreze, M. C., and J. A. Maslanik (1997), Arctic precipitation as represented in the NCEP/NCAR reanalysis, *Ann. Glaciol.*, *25*, 429–433.
- Serreze, M. C., J. A. Maslanik, T. A. Scambos, F. Fetterer, J. Stroeve, K. Knowles, C. Fowler, S. Drobot, R. G. Barry, and T. M. Haran (2003), A record minimum arctic sea ice extent and area in 2002, *Geophys. Res. Lett.*, *30*(3), 1110, doi:10.1029/2002GL016406.
- Serreze, M. C., A. P. Barrett, A. G. Slater, M. Steele, J. Zhang, and K. E. Trenberth (2007a), The large-scale energy budget of the Arctic, *J. Geophys. Res.*, *112*, D11122, doi:10.1029/2006JD008230.
- Serreze, M. C., M. M. Holland, and J. Stroeve (2007b), Perspectives on the Arctic's shrinking sea-ice cover, *Science*, *316*, 1533–1536, doi:10.1126/science.1139426.
- Serreze, M. C., A. P. Barrett, J. Stroeve, D. N. Kindig, and M. M. Holland (2009), The emergence of surface based Arctic amplification, *Cryosphere*, *3*, 11–19, doi:10.5194/tc-3-11-2009.
- Stroeve, J., M. C. Serreze, S. Drobot, S. Gearheard, M. M. Holland, J. A. Maslanik, W. Meier, and T. A. Scambos (2008), Arctic sea ice extent plummets in 2007, *Eos Trans. AGU*, *89*(2), 13, doi:10.1029/2008EO020001.
- Stroeve, J., M. C. Serreze, M. M. Holland, J. E. Kay, J. Maslanik, and A. P. Barrett (2011), The Arctic's rapidly shrinking sea ice cover: A research synthesis, *Clim. Change*, *110*(3–4), 1005–1027, doi:10.1007/s10584-011-0101-1.
- Sturm, M., and R. Massom (2010), Snow and sea ice, in *Sea Ice*, edited by D. N. Thomas and G. S. Dieckmann, p. 621, Blackwell, Oxford, U. K.
- Sturm, M., J. Holmgren, and D. K. Perovich (2002), Winter snow cover on the sea ice of the Arctic Ocean at the surface heat budget of the Arctic

- Ocean (SHEBA): Temporal evolution and spatial variability, *J. Geophys. Res.*, 107(C10), 8047, doi:10.1029/2000JC0000400.
- Sturm, M., J. A. Maslanik, D. K. Perovich, J. Stroeve, J. A. Richter-Menge, T. Markus, J. Holmgren, J. F. Heinrichs, and K. Tape (2006), Snow depth and ice thickness measurements from the Beaufort and Chuckchi Seas collected during the AMSR-Ice03 campaign, *IEEE Trans. Geosci. Remote Sens.*, 44(11), 3009–3020, doi:10.1109/TGRS.2006.878236.
- Thorndike, A. S., D. S. Rothrock, G. A. Maykut, and R. Colony (1975), The thickness distribution of sea ice, *J. Geophys. Res.*, 80, 4501–4513, doi:10.1029/JC080i033p04501.
- Toyota, T., S. Takatsuji, K. Tateyama, K. Naoki, and K. I. Ohshima (2007), Properties of sea ice and overlying snow in the Southern Sea of Okhotsk, *J. Oceanogr.*, 63, 393–411, doi:10.1007/s10872-007-0037-2.
- Vancoppenolle, M., T. Fichefet, H. Goose, S. Bouillon, G. Madec, and M. A. Morales Maqueda (2009), Simulating the mass balance and salinity of Arctic and Antarctic sea ice: 1: Model description and validation, *Ocean Modell.*, 27(1–2), 33–53, doi:10.1016/j.ocemod.2008.10.005.
- Wadhams, P. (1981), Sea ice topography of the Arctic Ocean on the region 70, *Philos. Trans. R. Soc. London A*, 302(1464), 45–85, doi:10.1098/rsta.1981.0157.
- Warren, S. G., I. G. Rigor, N. Untersteiner, V. F. Radionov, N. N. Bryazgin, Y. I. Aleksandrov, and R. Colony (1999), Snow depth on Arctic Sea ice, *J. Clim.*, 12, 1814–1829, doi:10.1175/1520-0442(1999)012<1814:SDOASI>2.0.CO;2.
- Winton, M. (2011), Do climate models underestimate the sensitivity of Northern Hemisphere sea ice cover?, *J. Clim.*, 24, 3924–3934, doi:10.1175/2011JCLI4146.1.
- Zhang, J., and D. A. Rothrock (2001), A thickness and enthalpy distribution sea-ice model, *J. Phys. Oceanogr.*, 31(10), 2896–3001, doi:10.1175/1520-0485(2001)031<2986:ATAEDS>2.0.CO;2.
- Zhang, J., I. W. D. Hibler, M. Steele, and D. A. Rothrock (1998), Arctic ice-ocean modeling with and without climate restoring, *J. Phys. Oceanogr.*, 28, 191–217, doi:10.1175/1520-0485(1998)028<0191:AIOMWA>2.0.CO;2.
- Zwally, H. J., et al. (2002), ICESat’s laser measurements of polar ice, atmosphere, ocean, and land, *J. Geodyn.*, 34, 405–445, doi:10.1016/S0264-3707(02)00042-X.